



Geophysical Research Letters[®]



RESEARCH LETTER

10.1029/2023GL104547

Prevalence of Deformation-Scale Surface Currents

A. Palóczy¹  and J. H. LaCasce¹ 

¹University of Oslo, Oslo, Norway

Key Points:

- We present a census of the widths of several surface jets across the global ocean, using in situ and satellite data
- Most jets are asymmetrical, with the half-widths correlated with the first surface radius on each side of the jet
- The asymmetry and deformation scale dependence are predicted by simple layered analytical models and reflect active lateral mixing

Supporting Information:

Supporting Information may be found in the online version of this article.

Correspondence to:

A. Palóczy,
a.p.filho@geo.uio.no

Citation:

Palóczy, A., & LaCasce, J. H. (2023). Prevalence of deformation-scale surface currents. *Geophysical Research Letters*, 50, e2023GL104547. <https://doi.org/10.1029/2023GL104547>

Received 15 MAY 2023

Accepted 7 SEP 2023

Abstract Understanding the transport of large ocean currents, like the Gulf Stream, has been of interest since the early days of oceanography. There has been less attention on the widths of the currents, although there exist several theoretical predictions. We present a census of time-averaged jet profiles, using in situ and satellite data. The jets are typically asymmetrical, being narrower on the side with weaker stratification. The half-widths L_j are correlated with the local deformation radius L_d associated with the first surface mode on either side. The dependence of L_j on L_d is predicted by simple shallow water geostrophic adjustment models, with or without outcropping layers. This implies that potential vorticity is well-mixed adjacent to the jets, due most likely to mesoscale eddies. The findings suggest that surface jet widths are determined locally, by eddy-mean flow interactions.

Plain Language Summary Narrow, persistent currents a few tens of kilometers wide are found in several regions of the ocean, like fast-flowing rivers. The Gulf Stream and Kuroshio are familiar examples. We use different measurements to show that these currents have a generic shape, being asymmetric relative to their point of maximum velocity, that is, they are wider on one side and narrower on the other. The profile has a distinctive shape and results from strong eddy stirring on either side of the jet. The jet widths depend on the local density profile and on the Earth's rotation.

1. Introduction

Narrow, mesoscale surface jets are common in the World Ocean. Examples include the Western Boundary Currents (WBCs), such as the Gulf Stream (GS), Kuroshio, Agulhas, Brazil and East Australian Currents (EAC). These are important elements of the climate system, transporting heat and other properties (e.g., Hu et al., 2015; Li et al., 2022). Other jets are found in the Antarctic Circumpolar Current (ACC, e.g., Lenn et al., 2007; Y. Firing et al., 2011; Xu et al., 2020) or locked to steep topographic slopes, such as the Antarctic Slope Current (e.g., Peña-Molino et al., 2016; Azaneu et al., 2017; Thompson et al., 2020) and the shelfbreak jet along the Middle Atlantic Bight (e.g., Fratantoni et al., 2001).

There has been much attention to what determines the transport of the major jets. For example, the Sverdrup transport, derived from integrating the wind stress curl across the North Atlantic, yields a reasonable estimate for the GS transport in the Florida Straits (e.g., Gill, 1982; Czeschel et al., 2012). But there is also the question of the *width* of the currents. Surface jets are barriers to lateral mixing (e.g., Bower et al., 1985; Samelson, 1992) and sites of isopycnal upwelling and subduction (e.g., Spall, 1995; Gille et al., 2022), so the jets' lateral structure is important for cross-stream tracer transport, water mass transformation and ventilation of the deep ocean.

A number of theoretical predictions exist. In Stommel (1948)'s seminal model of the GS, the width $L_S = r/\beta$ depends on the bottom friction coefficient, r , and the meridional gradient of the planetary vorticity, β . Munk (1950)'s model is similar but employs lateral (eddy) diffusion instead; the width, $L_M = (A_h/\beta)^{\frac{1}{3}}$, depends on the lateral viscosity, A_h . However, Munk's model requires large values of A_h to yield a realistic GS width. This prompted Charney (1955) to propose a nonlinear model. The resulting jet width, $L_i = (U_i/\beta)^{\frac{1}{2}}$, depends on β and the velocity in the Sverdrup interior, U_i . All three models are barotropic (depth-invariant) and thus exclude baroclinic effects. Parsons (1969) derived a two layer model of the GS, to understand how the current separates from the western boundary. In the frictional and inertial limits, the widths are consistent with the previous models.

On the other hand, the width could reflect nonlinear eddy-mean flow interactions. Eddy momentum fluxes tend to sharpen jets which are too broad and to widen jets which are too narrow (e.g., Held & Andrews, 1983). In a study of topographic effects on jet stability, Palóczy and LaCasce (2022) found that the momentum fluxes were near zero when the jet half-width was roughly 1.1–2 times the deformation radius (L_d). A similar prediction

© 2023. The Authors.

This is an open access article under the terms of the Creative Commons Attribution-NonCommercial-NoDerivs License, which permits use and distribution in any medium, provided the original work is properly cited, the use is non-commercial and no modifications or adaptations are made.

follows from the argument that eddies tend to homogenize potential vorticity (PV) on the jet flanks. Such mixing produces sharp PV gradients at the jet core with constant PV on the flanks, yielding a so-called “PV staircase” (Marcus & Lee, 1998; Nakamura, 1999; Dritschel & McIntyre, 2008, hereafter DM08). In the baroclinic case, the resulting jets have a half-width of L_d . A more elaborate model, due to Esler (2008), incorporating PV homogenization on the jet flanks and minimum potential energy, also predicts a jet half-width of L_d .

There are few observational studies of jet widths, but these are in accord with deformation scale jets. Such was the case in the study of the GS by Rossby and Zhang (2001, hereafter RZ01) at 37°N, downstream of where the current separates from the coast. Significantly, the current was found to be asymmetric, being narrower on the inshore side. The width on each side of the jet maximum was shown to scale with the local L_d ; as the thermocline is shallower on the inshore side, L_d is smaller there. They also found that the PV was nearly constant on the jet flanks, which they attributed to eddy stirring. The findings were supported by those of Archer et al. (2018, hereafter A18), who examined surface velocity profiles in the EAC and Florida Current (FC). The profiles were strikingly similar, indicating asymmetric jets with half-widths of the local L_d .

Are these findings typical of other surface jets? Hereafter we use a combination of satellite altimetry and direct shipboard velocity measurements (Section 2) to show that they may well be (Section 3). We also discuss a simple framework for the observed structure (Sections 4 and 5), and summarize our results and conclusions in Section 5.

2. Data

The data include satellite altimetry and repeat shipboard acoustic Doppler current profiles (ADCP). Figure 1 shows an overview of all data sets, with the locations of different surface jets indicated by the dots and boxes in Figure 1a. To average the velocities, we define a time-dependent, jet-following reference frame with the origin at the jet's core (e.g., RZ01, A18, Halkin & Rossby, 1985; Waterman et al., 2011; Delman et al., 2015; Archer et al., 2017). We do this both for the cross-track surface geostrophic velocity derived from the satellite altimetry data and the shipboard ADCP data (averaged in the upper 50 m). This avoids the smearing that would be introduced by current meandering in a geographically fixed reference frame.

2.1. Satellite Altimetry

To examine the structure of the absolute geostrophic velocity across different surface currents, we interpolate the gridded (1 min resolution) Mean Dynamic Topography (MDT) DTU15 product distributed by the Technical University of Denmark (Andersen & Knudsen, 2009) to the ground tracks of a multi-satellite merged Sea Surface Height Anomaly product (TPJAOS) distributed by the Physical Oceanography Distributed Active Archive Data Center (PODAAC, Beckley et al., 2010). This product spans the 1993–2021 period and has an along-track resolution of ≈ 5.8 km, with a temporal resolution of ≈ 10 days (repeat time of each altimeter cycle). We use the resulting time series of along-track Absolute Dynamic Topography (hereafter L2ADT) crossing surface currents in different ocean basins to derive cross-track surface geostrophic velocities. Specifically, we first use the DTU15 MDT to find locations with high mean surface geostrophic speeds, and choose the nearest altimeter ground track from the TPJAOS product with a crossing angle as close to perpendicular to the jet's axis as possible (e.g., five ground-tracks crossing the GS are shown in Figure 1b). Along these transects, we compute the surface cross-track geostrophic velocity. We first find the location where the ADT gradient is largest by fitting a ninth degree polynomial to the L2ADT data, and then shift the ADT profile accordingly. Next, we use the daily, Optimally-Interpolated ADT distributed by the Copernicus Marine Environment Monitoring Service (CMEMS, hereafter L4ADT, Pujol et al., 2016) to determine the orientation of the jet relative to the fixed L2ADT ground track, and project the cross-track velocity derived from the L2ADT on the jet direction. Thus we follow each jet as it develops meanders and eddies.

2.2. Shipboard ADCP Data

We use data from a 150 kHz ADCP installed on the Antarctic Research and Supply Vessel Laurence M. Gould (LMG), a vessel that regularly crosses Drake Passage between southern South America and Palmer Station in the Antarctic Peninsula. We focus here on the shelf break jet at the northern end of Drake Passage, the Cape Horn Current (CHC, Acha et al., 2004; Bouali et al., 2017), and on the ACC jets collocated with the Subantarctic

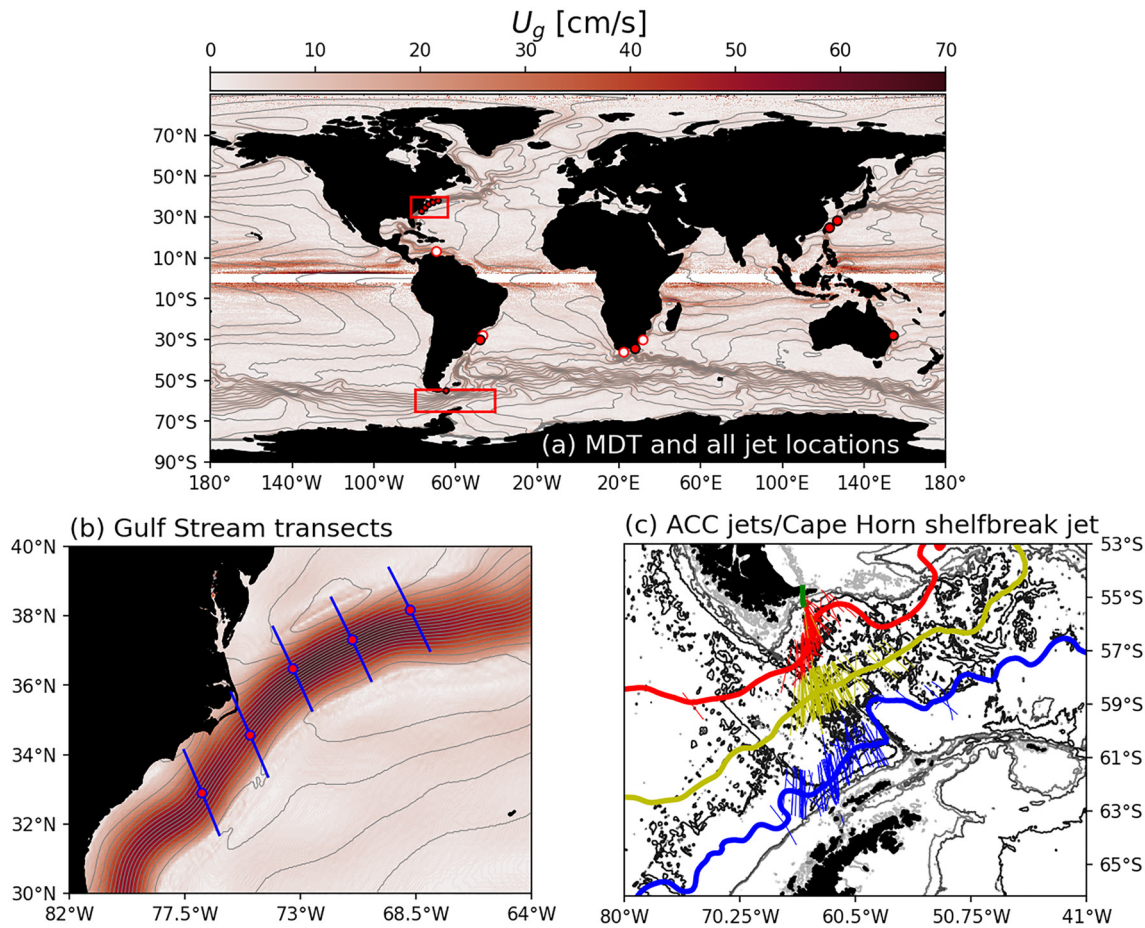


Figure 1. Satellite and shipboard data sets in different ocean basins. (a) Time-mean surface absolute geostrophic speed U_g (color scale, masked within $\pm 2^\circ$ of the equator) and MDT contours from the DTU15 product. The red dots indicate the satellite ground tracks and the CHC ADCP transect positions used to calculate time-averaged jet profiles, while the red boxes delimit two of the regions examined: The GS (b) and Drake Passage (c). The red circles locate the synoptic GO-SHIP jets. The blue lines on panel (b) are the ground track segments used to derive GS jet profiles (the three segments farther northeast are downstream of separation). The U_g color scale is the same on panels (a) and (b). The green segment on panel (c) indicates the CHC, while the thick red, yellow and blue lines are the climatological positions of the SAF, PF and SACCF from Park et al. (2019). The thin red, yellow and blue lines are the individual ship crossings of each ACC frontal jet. The gray contours are the 100, 1,000, 2,000, and 4,000 m isobaths from the SRTM15+ data set (Tozer et al., 2019).

Front, the Polar Front, and the Southern ACC front (SAF, PF and SACCF, Figure 1c, e.g., Sprintall, 2003; Lenn et al., 2007). Expendable Bathythermograph (XBT) profiles are also used to derive associated cross-stream temperature and Ertel PV profiles for the CHC. The LMG ADCP data were processed with the Common Ocean Data Access System (CODAS) framework (E. Firing & Hummon, 2010; E. Firing et al., 2012) yielding averaged velocities at an along-track resolution of ≈ 1.5 km, and projected on a stream-following coordinate system based on the individual surface jets identified in the data. Both the ADCP and XBT LMG data sets are described by Gutierrez-Villanueva et al. (2020). For the ACC jets, we use the daily CMEMS L4ADT maps to determine the orientation of the jets at each ship crossing and rotate the ADCP velocity accordingly, while for the CHC (and the GO-SHIP jets described below) we use the direction of the velocity vector averaged within ± 10 km of the core. The time-varying ACC jet positions are derived from finding the maximum speed within 100 km of the point where each ship track intersects Park et al. (2019)'s MDT-derived climatological ACC front positions (red, yellow and blue lines on Figure 1c). Note that the poleward flank of the SACCF jet sometimes touches the Antarctic continental slope.

We also use ADCP data from individual GO-SHIP lines crossing the Agulhas, Brazil and Guianas Currents (Figure S1 in Supporting Information S1) to add more velocity profiles to our analysis. Unlike the LMG ADCP data, these transects are not occupied frequently enough to enable time-averaging, but are useful because they sample surface jets that are difficult to derive from altimetry due to the angle between the satellite ground track and the jet's orientation.

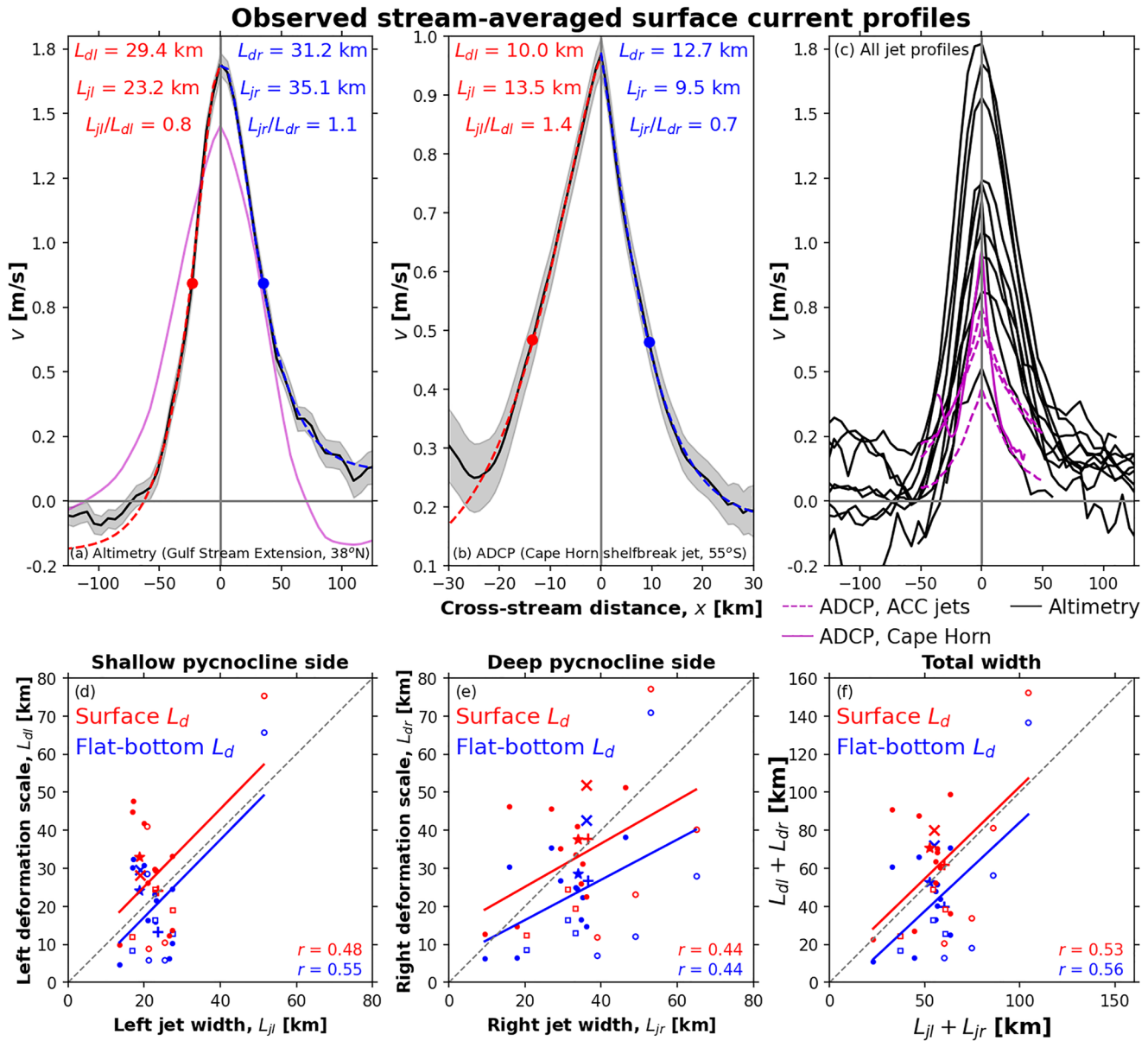


Figure 2. (a–c): Observed time-averaged, near-surface jet profiles in stream-following coordinates. (a) GS Extension jet at 38°N derived from along-track altimetry (L2ADT). The magenta line is the associated velocity profile from lower-resolution L4ADT maps. (b) CHC at 55°S derived from LMG ADCP data. (c) All observed time-averaged jet profiles. All profiles are plotted such that the left side ($x < 0$) is the shallow pycnocline flank. Red and blue dashed lines on (a, b) are the double-exponential fits on either side. The associated left/right half-widths L_{jl}/L_{jr} are the red/blue dots. The gray shading indicates \pm twice the standard errors. The black and magenta curves on (c) are respectively the altimetry- and ADCP-derived jet profiles. The dashed curves are the ACC jets. (d–f): Surface jet widths L_j versus local deformation scale L_d for all observed currents, with associated linear regression lines. Panels (d, e, f) are respectively the left (shallow pycnocline flank), right (deep pycnocline flank), and total jet width versus local L_d . The open circles are the synoptic GO-SHIP jets (Figure S1 in Supporting Information S1), and the open squares are the ACC jets. The stars are data from RZ01 across the GS. The “+” and “x” markers are data from A18 for the FC and EAC, respectively. Red (blue) is based on the first surface (flat bottom) L_d , interpolated from LG20’s global map. The gray dashed line is the 1:1 line. All correlation coefficients are significant at the 99% confidence level following the Student’s t -test.

3. Observed Time-Mean Velocity Profiles

We begin by examining the cross-stream time-averaged structure of all the available surface jet profiles. Figures 2a and 2b shows two examples: the GS near 38°N and the CHC. The left-right asymmetry is evident in both cases, and as in the other currents close to a continental slope, the inshore width is smaller (Figure 2c). The CHC (Figure 2b) is the only exception, with the inshore and more linear flank being slightly wider. Following the form

of the solution for a theoretical model (Section 4) and similar to RZ01, we fit a combination of two exponentials to each side of the jet. The fit is constrained to coincide with the velocity at the jet core and the data is trimmed at the point where the velocity is 10% of the core value on either side (or a point close to the value farthest from the jet core if the profile does not sample the 10% point).

The asymmetry is quantified by the half-widths L_{jl} and L_{jr} on the left and right flanks of each jet. We define the half-widths as the points where the velocity is 50% of the core velocity. For comparison with the jet half widths, we interpolated LaCasce and Groeskamp (2020, hereafter LG20)'s L_d values associated with the first surface mode. Surface modes are similar to the traditional baroclinic modes, except that the ocean bottom is assumed to be rough rather than flat. Surface modes compare more favorably with observations from current meters and satellite altimetry (de La Lama et al., 2016, LG20) than flat bottom modes. The first surface radius values were interpolated to the altimeter or ship tracks and averaged on either side between the jet core and the 50% point.

Plotting the velocity profiles of all surface jets reveals widths spanning the range ≈ 20 –100 km, with peak velocities of ≈ 0.5 –1.75 m/s (Figure 2c). The finer-resolution ADCP data resolve the narrower, higher-latitude ACC jets and the CHC (magenta curves in Figure 2c). The altimeter-derived velocities have smoother cores, but clearly resolve the structure of the jets, unlike the L4ADT product (magenta line on panel a), which has an effective midlatitude resolution of ≈ 200 km (Ballarotta et al., 2019). The left-right asymmetry is clear in most jets, especially in those locked to bathymetry. The ACC jets (dashed magenta curves in Figure 2c) are the clearest exceptions: They are more symmetric and far from continental margins. The left-right L_d difference is less than 0.5 km for all three jets, consistent with theory (see Section 4).

To quantify the dependence, we plotted the observed jet widths against L_d , both surface and flat bottom (Figures 2d–2f), for all 21 available velocity profiles. These represent the 14 time-averaged jets resolved in the analysis, plus the 4 synoptic jets from GO-SHIP lines (Figure S1 in Supporting Information S1), RZ01's GS profile and A18's FC and EAC profiles. The scatterplots for the left (shallower pycnocline) and right (deeper pycnocline) jet flanks are shown in Figures 2d and 2e. In the latter, the jet tends to be slightly wider than L_d , but the jet half-widths are significantly correlated with the L_d , in both cases. Comparing the sum of the left and right surface L_d against the total width yields a correlation coefficient of 0.53–0.56 (Figure 2f). Choosing the 55% (45%) point instead decreases (increases) the correlations in Figure 2f by up to 0.11 (0.02). Excluding the three ACC jets reduces the correlations by 0.02–0.03, and excluding the four synoptic jets reduces the correlations by 0.24–0.25. The correlations obtained with either the surface or the flat bottom radii are all significantly different from zero at the 99% confidence level, but are statistically indistinguishable from each other with the 21 degrees of freedom available.

The limitations of the L_d maps (including not being in a jet-following frame and deriving from a density climatology which uses an isotropic objective mapping scheme) affect the correlations. Calculating the left (right) surface L_d directly from the stream-averaged CHC XBT data (Figure 3a) yields 6.3 (8.3) km, instead of 10 (12.7) km (Figure 2b). Additionally, the rotation assumes that there is no along-stream variation in the velocity field across the footprint of the rotation angle, and there is uncertainty in the rotation angle itself, because it comes from the smooth L4ADT altimetry product.

As with the GS in RZ01, the near-surface PV exhibits a nearly step-wise distribution in the time-averaged CHC (Figure 3b). In the GS case, the PV is dominated by the layer thickness component (RZ01's Figure 13), while here, the relative vorticity contribution is important on the inshore flank. This may be because the interface displacement is gentler than in the GS (compare Figure 3a with e.g., RZ01's Figure 12). The PV structure in many of the other jets is likely similar to the GS's, where persistent vertical isopycnal displacements of O(100 m) are commonly observed across the jet core.

4. Rationalizing the Jet Widths

The double-exponential asymmetrical velocity profile can be predicted using geostrophic adjustment (e.g., Cushman-Roisin & Beckers, 2011; Vallis, 2017) in a 1.5 layer shallow water model. Assuming an initial step-wise pycnocline displacement (the dashed contour in Figure 3d) and no motion, the interface relaxes to a smooth curve, balanced by a perpendicular geostrophic flow. The adjusted interfacial profile can be predicted by conservation of PV:

$$\frac{f}{H} = \frac{f + v_x}{H - \eta}, \quad (1)$$

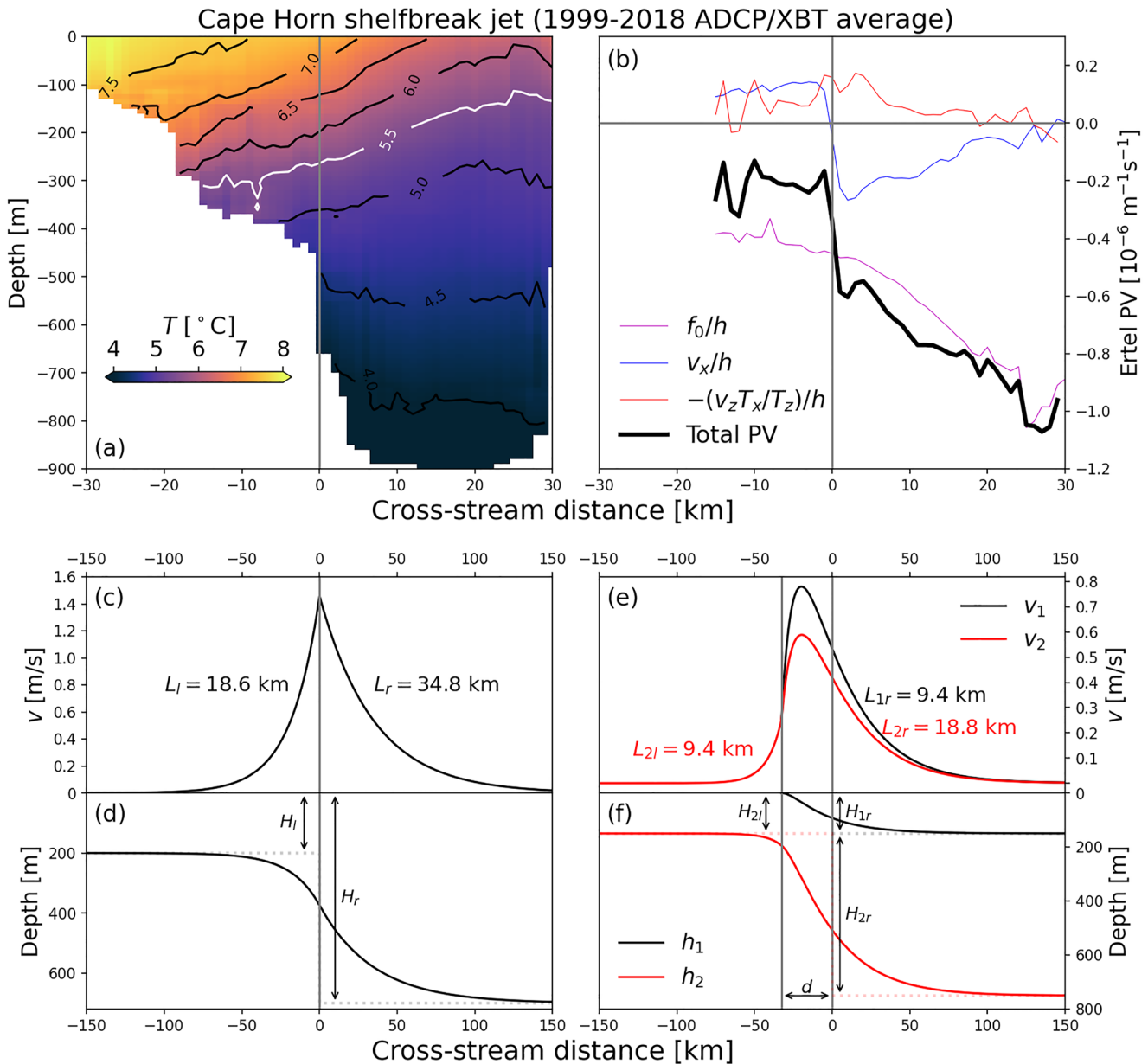


Figure 3. Observed time-averaged temperature and Ertel PV for the CHC from ADCP/XBT data. (a) Temperature (proxy for density) averaged in the same stream-following frame as that used to obtain the velocity profile in Figure 2b, showing isotherm/isopycnal outcropping. (b) Total Ertel PV (black line) and its individual components (magenta, red and blue lines) showing a PV jump across the jet's core. The 5.5°C isotherm is used as the interface. (c–f) Schematic representation of the reduced-gravity shallow water geostrophic adjustment models for a generic jet with a PV discontinuity across its core. (c, d) 1.5 layer without outcropping, with H_l , H_r values based on RZ01's measurements across the GS (their Figure 12). (e, f) 2.5 layers with outcropping top layer. Both layered models predict asymmetrical jets with half-widths proportional to the deformation radii based on the layer thicknesses on each side of the jet (see Supporting Information S1).

where x is the cross-stream coordinate, $g' = g(\rho_2 - \rho_1)/\rho_2$ is the reduced gravity based on the active upper and stagnant lower layer densities, v_x is the relative vorticity of the jet, $H(x)$ is the initial (step-like) interfacial profile, and $\eta(x)$ is the final departure from $H(x)$. The resulting asymmetrical jet profile is given by:

$$v(x) = \frac{g'(H_r - H_l)}{f(L_r + L_l)} \exp(-|x|/L_{l,r}) \quad (2)$$

where H_l and H_r are respectively the interface depths on the left and right sides, and the associated deformation radii are:

$$L_l, L_r = \sqrt{g'H_l/f}, \sqrt{g'H_r/f}, \quad (3)$$

where $L_{l,r}$ indicates L_l on the left side and L_r on the right. Thus geostrophic adjustment predicts an asymmetric jet with deformation-scale flanks (Figures 3c and 3d).

While some jets exhibit clear exponential dependence on one (e.g., right side in Figure 2b) or both sides, others are rounded near the velocity maximum and some exhibit a more linear dependence on one flank (e.g., left side in Figure 2b). The GS jet in Figure 2a is an example. A single-exponential velocity profile predicted by the 1.5-layer geostrophic adjustment model yields a poor fit here and in many of the other jets (not shown).

But more general observed profiles can be obtained with a slightly more complicated model. In particular, one can add an *outcropping* layer on the more stratified side, yielding a so-called “2.5 layer” model on that side. Outcropping of deeper isopycnals is seen for many of the jets examined here (e.g., the CHC and the ACC jets), and the presence of a mixed layer means that any surface jet will have some degree of outcropping, even if it is a thin layer. The model is more complicated to solve analytically but is still tractable (see derivation in Supporting Information S1). The resulting jets are also asymmetrical, but exhibit more complex structure depending on the choices of resting layer thicknesses.

An example is shown in Figures 3e and 3f. The velocity near the jet maximum is rounded near the region where the top layer outcrops. Also, the profile is less obviously exponential on either side of the jet; indeed, it is nearly linear on the right side. Thus a profile like that of the GS in Figure 2a can be obtained with such an outcropping model. But it also yields more exponential profiles if the outcropping layer is thinner (Figure S2 in Supporting Information S1). Thus the 2.5 layer model appears to be the simplest which can capture the range of profiles seen in the data.

The 2.5 layer solution, a combination of exponentials, is too complex to facilitate simple curve-fitting. For this reason, we employed a linear combination of two exponentials on each flank (a function of the form $v_{\text{fit}}(x) = ae^{-|x|/L_1} + be^{-|x|/L_2} + c$, where a , b , c , L_1 , and L_2 are free parameters) with the observed core profiles (e.g., Figures 2a and 2b). This yielded reasonable fits in most cases.

The rounded profile near the jet maximum was also described by RZ01. They accounted for this by fitting two exponentials on each side, one for the inner profile and one for the outer. They suggested the rounding was due to lateral stirring near the jet maximum. Here we see that such a profile can obtain without such interior mixing, provided that isopycnal outcropping occurs.

There is an additional aspect of the model. Because PV is conserved in the calculation, the PV in the final state is the same step-wise distribution assumed for the initial state (Figures 3d and 3f). Thus an alternate way to view the jet is as a geostrophically-balanced flow lying between two regions with homogenized PV, that is, a PV “staircase” (Marcus & Lee, 1998, DM08). As suggested by RZ01, this would be expected with vigorous lateral stirring on the flanks, by mesoscale eddies for example,

Lastly, we note that the deformation radii in the 1.5 and 2.5 layer models correspond to *surface* radii, because there is no flow in the bottom layer. So it is natural to compare the jet widths to surface radii, rather than flat bottom radii.

5. Summary and Discussion

Previous observational studies of the GS (Halkin & Rossby, 1985, RZ01), the FC, and the EAC (Archer et al., 2017, A18) revealed that their time-averaged surface velocity profiles are asymmetrical, with half-widths similar to the local baroclinic deformation radius L_d . By compiling velocity profiles from several surface currents in different ocean basins (Figure 1), we find that this asymmetry and dependence on the local L_d is likely ubiquitous, with currents being ≈ 20 –100 km wide (Figure 2).

Both the quasi-exponential shape and the widths of the observed time-averaged velocity profiles are predicted by simple layered geostrophic adjustment models (Figures 3c–3f and Supporting Information S1). The models are equivalent to a PV inversion, assuming that the PV is constant on either side of the jet as a result of eddy stirring.

When taking the finite depth change across the jet into account, one obtains an asymmetric jet. And a model with layer outcropping predicts jet profiles which are not strictly exponential, but rounded near the maximum and even approximately linear on one flank, as seen in many of the examples here (Figures 2a–2c). This paradigm emphasizes the importance of local eddy-mean flow interactions in setting the lateral scale of surface mesoscale jets.

While they did not make the explicit connection to the geostrophic adjustment problem, many of the essential points were made by RZ01 regarding the GS jet from the Oleander ADCP data set. The jet half-widths were linked to the L_d on either side and the upper layer PV, that is, that above the 1.027 kg/m³ isopycnal, was nearly constant on the jet flanks. The results are also in line with linear baroclinic models which predict neutral momentum fluxes when the jet half-width is deformation scale (Held & Andrews, 1983; Palóczy & LaCasce, 2022), and with nonlinear models which assume PV homogenization on the jet flanks (Nakamura, 1999; Esler, 2008, DM08). Geostrophic adjustment models, like those considered here, are perhaps the simplest to exhibit the relevant characteristics.

We tested other predictions for the jet width as well. Stommel's and Munk's models are linear and require large damping coefficients to produce realistic jet widths. Charney's inertial boundary scaling $L_i = (U_i/\beta)^{\frac{1}{2}}$ predicts the width to be proportional to the velocity scale for the Sverdrup interior flow, U_i . This scale is very similar for the different jets examined here, so the predicted jet widths depend primarily on latitude, through β . Comparing L_i with the observed widths for the subset of the WBCs in our analysis yielded poor correlations (not shown). Furthermore, all three of these models are barotropic and predict symmetric jets, while the observations clearly show asymmetric, deformation-scale jets.

The results imply that General Circulation Models must at least resolve the deformation radius to simulate jet dynamics correctly. With coarser resolution, as is typical for example, in current climate models, the relevant momentum fluxes are almost certainly not captured. This likely impacts how the models represent processes like cross-jet mixing, subduction and the ventilation of the deep ocean.

Acknowledgments

AP and JHL acknowledge support from The Rough Ocean Project, funded by the Research Council of Norway under the Klimaforsk-programme, project #302743. This study has been conducted using E.U. Copernicus Marine Service Information; DOI <https://doi.org/10.48670/moi-00145>. We thank the United States National Science Foundation (NSF)'s Office of Polar Programs Antarctic Division (ANT) for support of the Drake Passage time series through Grants OPP-9816226, ANT-0338103, ANT-0838750, PLR-1341431, PLR-1542902 and ANT-2001646 and the Chereskin Lab at Scripps Institution of Oceanography/UCSD (<http://adcp.ucsd.edu/lmgould/>), for maintaining the collection, processing and dissemination of the ARSV Laurence M. Gould (LMG) ADCP data. We also thank Eric Firing and Jules Hummon (University of Hawaii) for their support of underway ADCP data through the UHDAS/CODAS software and the Joint Archive of Shipboard ADCP Data (JASADCP). We are grateful to the scientists and technicians onboard the LMG and R/Vs Ronald H. Brown, Atlantis and Thomas G. Thompson for ADCP data collection. Acquisition and processing of the GO-SHIP ADCP measurements has been funded by NSF Grants OCE-0223505, OCE-0752970, and OCE-1437015. The XBT data were made available by the Scripps High Resolution XBT program (www-hrx.ucsd.edu). We thank the two anonymous reviewers for their input, which substantially improved the manuscript. We also thank Jonathan Lilly for creating the reformatted version of the TPJAOS data set. Early discussions with Sarah Gille and Tom Rossby were very helpful.

Data Availability Statement

Code required to reproduce the results and figures is available at <https://github.com/apaloczy/SurfaceOceanJets>, archived under <https://doi.org/10.5281/zenodo.8339373> (Palóczy, 2023). The objectively-mapped Absolute Dynamic Topography product is distributed by the Copernicus Marine Environment Monitoring Service (CMEMS, 2023). The DTU15 Mean Dynamic Topography is distributed by the Technical University of Denmark (DTU, 2015). The merged along-track sea surface height anomaly TPJAOS data set is distributed by NASA/PODAAC (Beckley et al., 2022), and the reformatted version used in this study was created by Lilly (2022). The Park et al. (2019) climatological Antarctic Circumpolar Current front positions data set was created by Park and Durand (2019). The SRTM15+ bathymetry data set is distributed by IGPP (2023). The ARSV Laurence M. Gould (LMG) underway ADCP velocity data set is distributed by JASADCP (2022). The LMG underway XBT temperature data set is distributed by the Scripps High Resolution XBT program (HRX, 2022). The GO-SHIP underway ADCP velocity data sets are distributed by GO-SHIP (2023).

References

- Acha, E. M., Mianzan, H. W., Guerrero, R. A., Favero, M., & Bava, J. (2004). Marine fronts at the continental shelves of austral South America: Physical and ecological processes. *Journal of Marine Systems*, 44(1), 83–105. <https://doi.org/10.1016/j.jmarsys.2003.09.005>
- Andersen, O. B., & Knudsen, P. (2009). DNSC08 mean sea surface and mean dynamic topography models. *Journal of Geophysical Research*, 114(C11), C11001. <https://doi.org/10.1029/2008JC005179>
- Archer, M. R., Roughan, M., Keating, S. R., & Schaeffer, A. (2017). On the variability of the East Australian Current: Jet structure, meandering, and influence on shelf circulation. *Journal of Geophysical Research*, 122(11), 8464–8481. <https://doi.org/10.1002/2017JC013097>
- Archer, M. R., Keating, S. R., Roughan, M., Johns, W. E., Lumpkin, R., Beron-Vera, F. J., & Shay, L. K. (2018). The kinematic similarity of two western boundary currents revealed by sustained high-resolution observations. *Geophysical Research Letters*, 45(12), 6176–6185. <https://doi.org/10.1029/2018GL078429>
- Azaneu, M., Heywood, K. J., Queste, B. Y., & Thompson, A. F. (2017). Variability of the Antarctic Slope Current system in the northwestern Weddell Sea. *Journal of Physical Oceanography*, 47(12), 2977–2997. <https://doi.org/10.1175/JPO-D-17-0030.1>
- Ballarotta, M., Ubelmann, C., Pujol, M.-I., Taburet, G., Fournier, F., Legeais, J.-F., et al. (2019). On the resolutions of ocean altimetry maps. *Ocean Science*, 15(4), 1091–1109. <https://doi.org/10.5194/os-15-1091-2019>
- Beckley, B. D., Zelensky, N., Holmes, S., Lemoine, F., Ray, R., Mitchum, G., et al. (2022). Integrated multi-mission ocean altimeter data for climate research complete time series Version 5.1. *NASA Physical Oceanography DAAC*. <https://doi.org/10.5067/ALTTS-TJA51>
- Beckley, B. D., Zelensky, N. P., Holmes, S. A., Lemoine, F. G., Ray, R. D., Mitchum, G. T., et al. (2010). Assessment of the Jason-2 extension to the TOPEX/Poseidon, Jason-1 sea-surface height time series for global mean sea level monitoring. *Marine Geodesy*, 33(1), 447–471. <https://doi.org/10.1080/01490419.2010.491029>

- Bouali, M., Sato, O. T., & Polito, P. S. (2017). Temporal trends in sea surface temperature gradients in the South Atlantic Ocean. *Remote Sensing of Environment*, 194, 100–114. <https://doi.org/10.1016/j.rse.2017.03.008>
- Bower, A. S., Rossby, H. T., & Lillibridge, J. L. (1985). The Gulf Stream—Barrier or blender? *Journal of Physical Oceanography*, 15(1), 24–32. [https://doi.org/10.1175/1520-0485\(1985\)015<0024:TGSOB>2.0.CO;2](https://doi.org/10.1175/1520-0485(1985)015<0024:TGSOB>2.0.CO;2)
- Charney, J. G. (1955). The Gulf Stream as an inertial boundary layer. *Proceedings of the National Academy of Sciences of the United States of America*, 41(10), 731–740. <https://doi.org/10.1073/pnas.41.10.731>
- CMEMS. (2023). Global ocean gridded L4 sea surface heights and derived variables reprocessed Copernicus climate service. <https://doi.org/10.48670/moi-00145>
- Cushman-Roisin, B., & Beckers, J.-M. (2011). *Introduction to geophysical fluid dynamics: Physical and numerical aspects*. Academic press.
- Czeschel, L., Eden, C., & Greatbatch, R. J. (2012). On the driving mechanism of the annual cycle of the Florida current transport. *Journal of Physical Oceanography*, 42(5), 824–839. <https://doi.org/10.1175/JPO-D-11-0109.1>
- de La Lama, M. S., LaCasce, J. H., & Fuhr, H. (2016). The vertical structure of ocean eddies. *Journal of Physical Oceanography*, 1(1), 1–16. <https://doi.org/10.1093/climsys/dzw001>
- Delman, A. S., McClean, J. L., Sprintall, J., Talley, L. D., Yulaeva, E., & Jayne, S. R. (2015). Effects of eddy vorticity forcing on the mean state of the Kuroshio extension. *Journal of Physical Oceanography*, 45(5), 1356–1375. <https://doi.org/10.1175/JPO-D-13-0259.1>
- Dritschel, D. G., & McIntyre, M. E. (2008). Multiple jets as PV staircases: The Phillips effect and the resilience of eddy-transport barriers. *Journal of the Atmospheric Sciences*, 65(3), 855–874. <https://doi.org/10.1175/2007JAS2227.1>
- DTU. (2015). Technical University of Denmark global 1 minute gridded mean dynamic topography. Retrieved from https://ftp.space.dtu.dk/pub/DTU15/I_MIN/
- Esler, J. G. (2008). The turbulent equilibration of an unstable baroclinic jet. *Journal of Fluid Mechanics*, 599, 241–268. <https://doi.org/10.1017/S0022112008000153>
- Firing, E., Hummon, J., & Chereskin, T. (2012). Improving the quality and accessibility of current profile measurements in the. *Southern Ocean*, 25(3), 164–165. <https://doi.org/10.5670/oceanog.2012.91>
- Firing, E., & Hummon, J. M. (2010). Shipboard ADCP measurements. In E. M. Hood, C. L. Sabine, & B. M. Sloyan (Eds.), *The GO-SHIP repeat hydrography manual: A collection of expert reports and guidelines*. IOCCP Report Number 14, ICPO Publication Series Number 134 Retrieved from <http://www.go-ship.org/HydroMan.html>
- Firing, Y., Chereskin, T., & Mazloff, M. (2011). Vertical structure and transport of the Antarctic circumpolar current in Drake Passage from direct velocity observations. *Journal of Geophysical Research*, 116(C8), C08015. <https://doi.org/10.1029/2011JC006999>
- Fratantoni, P. S., Pickart, R. S., Torres, D. J., & Scotti, A. (2001). Mean structure and dynamics of the shelf break jet in the middle Atlantic bight during fall and winter. *Journal of Physical Oceanography*, 31(8), 2135–2156. [https://doi.org/10.1175/1520-0485\(2001\)031<2135:MSADOT>2.0.CO;2](https://doi.org/10.1175/1520-0485(2001)031<2135:MSADOT>2.0.CO;2)
- Gill, A. E. (1982). *Atmospheric-ocean dynamics*. Academic Press.
- Gille, S. T., Sheen, K. L., Swart, S., & Thompson, A. F. (2022). Mixing in the Southern Ocean. In *Ocean mixing* (pp. 301–327). <https://doi.org/10.1016/b978-0-12-821512-8.00019-0>
- GO-SHIP (2023). Underway ADCP velocity measurements from the GO-SHIP program cruises (lines 2011_A10, 2012_A22, 2018_I07N and 2019_I06S). Retrieved from https://currents.soest.hawaii.edu/clivar_co2/index.html
- Gutierrez-Villanueva, M. O., Chereskin, T. K., & Sprintall, J. (2020). Upper-ocean eddy heat flux across the Antarctic Circumpolar Current in Drake Passage from observations: Time-mean and seasonal variability. *Journal of Physical Oceanography*, 50(9), 2507–2527. <https://doi.org/10.1175/JPO-D-19-0266.1>
- Halkin, D., & Rossby, T. (1985). The structure and transport of the Gulf Stream at 73°W. *Journal of Physical Oceanography*, 15(11), 1439–1452. [https://doi.org/10.1175/1520-0485\(1985\)015<1439:TSATOT>2.0.CO;2](https://doi.org/10.1175/1520-0485(1985)015<1439:TSATOT>2.0.CO;2)
- Held, I. M., & Andrews, D. G. (1983). On the direction of the eddy momentum flux in baroclinic instability. *Journal of the Atmospheric Sciences*, 40(9), 2220–2231. [https://doi.org/10.1175/1520-0469\(1983\)040<2220:OTDOTE>2.0.CO;2](https://doi.org/10.1175/1520-0469(1983)040<2220:OTDOTE>2.0.CO;2)
- HRX (2022). Underway XBT temperature measurements from the ARSV Laurence M. Gould. Scripps high resolution XBT program. Retrieved from <https://www-hrx.ucsd.edu/ax22.html>
- Hu, D., Wu, L., Cai, W., Gupta, A. S., Ganachaud, A., Qiu, B., et al. (2015). Pacific western boundary currents and their roles in climate. *Nature*, 522(7556), 299–308. <https://doi.org/10.1038/nature14504>
- IGPP. (2023). *Global bathymetry and topography at 15 arc sec*. (Satellite Geodesy Research Group at the Cecil H. and Ida M. Institute of Geophysics and Planetary Physics (IGPP), Scripps Institution of Oceanography, University of California San Diego (SIO/UCSD). Dataset version SRTM15+V2.5.5. Retrieved from https://topex.ucsd.edu/pub/srtm15_plus/
- JASADCP (2022). *Underway ADCP velocity measurements from the ARSV Laurence M. Gould*. Joint Archive for Shipboard ADCP (JASADCP). PI: Dr. Teresa Chereskin. Retrieved from <https://uhslc.soest.hawaii.edu/sadcp/INVENTORY/imgould.html>
- LaCasce, J. H., & Groeskamp, S. (2020). Baroclinic modes over rough bathymetry and the surface deformation radius. *Journal of Physical Oceanography*, 50(10), 2835–2847. <https://doi.org/10.1175/JPO-D-20-0055.1>
- Lenn, Y.-D., Chereskin, T., Sprintall, J., & Firing, E. (2007). Mean jets, mesoscale variability and eddy momentum fluxes in the surface layer of the Antarctic circumpolar current in Drake Passage. *Journal of Marine Research*, 65(1), 27–58. <https://doi.org/10.1357/002224007780388694>
- Li, J., Roughan, M., & Kerry, C. (2022). Drivers of ocean warming in the western boundary currents of the Southern Hemisphere. *Nature Climate Change*, 12(10), 901–909. <https://doi.org/10.1038/s41558-022-01473-8>
- Lilly, J. M. (2022). Sea surface height anomalies from the Beckley merged dataset. Retrieved from <http://www.jmlilly.net/ftp/pub/tpjaos.zip> http://www.jmlilly.net/doc/about_tpjaos.html
- Marcus, P. S., & Lee, C. (1998). A model for eastward and westward jets in laboratory experiments and planetary atmospheres. *Physics of Fluids*, 10(6), 1474–1489. <https://doi.org/10.1063/1.869668>
- Munk, W. H. (1950). On the wind-driven ocean circulation. *Journal of the Atmospheric Sciences*, 7(2), 80–93. [https://doi.org/10.1175/1520-0469\(1950\)007<0080:OTWDOC>2.0.CO;2](https://doi.org/10.1175/1520-0469(1950)007<0080:OTWDOC>2.0.CO;2)
- Nakamura, N. (1999). Baroclinic–Barotropic adjustments in a meridionally wide domain. *Journal of the Atmospheric Sciences*, 56(13), 2246–2260. [https://doi.org/10.1175/1520-0469\(1999\)056<2246:BBAIAM>2.0.CO;2](https://doi.org/10.1175/1520-0469(1999)056<2246:BBAIAM>2.0.CO;2)
- Palóczy, A. (2023). *apaloczy/SurfaceOceanJets: First release*. Zenodo. <https://doi.org/10.5281/zenodo.8339374>
- Palóczy, A., & LaCasce, J. H. (2022). Instability of a surface jet over rough topography. *Journal of Physical Oceanography*, 52(11), 2725–2740. <https://doi.org/10.1175/JPO-D-22-0079.1>
- Park, Y.-H., & Durand, I. (2019). *Altimetry-driven Antarctic Circumpolar Current fronts*. SEANOE. <https://doi.org/10.17882/59800>

- Park, Y.-H., Park, T., Kim, T.-W., Lee, S.-H., Hong, C.-S., Lee, J.-H., et al. (2019). Observations of the Antarctic Circumpolar current over the Udintsev fracture zone, the narrowest choke point in the Southern Ocean. *Journal of Geophysical Research*, *124*(7), 4511–4528. <https://doi.org/10.1029/2019JC015024>
- Parsons, A. T. (1969). A two-layer model of Gulf Stream separation. *Journal of Fluid Mechanics*, *39*(3), 511–528. <https://doi.org/10.1017/S0022112069002308>
- Peña-Molino, B., McCartney, M. S., & Rintoul, S. R. (2016). Direct observations of the Antarctic Slope Current transport at 113°E. *Journal of Geophysical Research*, *121*(10), 7390–7407. <https://doi.org/10.1002/2015JC011594>
- Pujol, M.-I., Faugère, Y., Taburet, G., Dupuy, S., Pelloquin, C., Ablain, M., & Picot, N. (2016). DUACS DT2014: The new multi-mission altimeter data set reprocessed over 20 years. *Ocean Science*, *12*(5), 1067–1090. <https://doi.org/10.5194/os-12-1067-2016>
- Rossby, T., & Zhang, H.-M. (2001). The near-surface velocity and potential vorticity structure of the Gulf Stream. *Journal of Marine Research*, *59*(6), 949–975. <https://doi.org/10.1357/00222400160497724>
- Samelson, R. M. (1992). Fluid exchange across a meandering jet. *Journal of Physical Oceanography*, *22*(4), 431–444. [https://doi.org/10.1175/1520-0485\(1992\)022<0431:FEAAMJ>2.0.CO;2](https://doi.org/10.1175/1520-0485(1992)022<0431:FEAAMJ>2.0.CO;2)
- Spall, M. A. (1995). Frontogenesis, subduction, and cross-front exchange at upper ocean fronts. *Journal of Geophysical Research*, *100*(C2), 2543–2557. <https://doi.org/10.1029/94JC02860>
- Sprintall, J. (2003). Seasonal to interannual upper-ocean variability in the Drake Passage. *Journal of Marine Research*, *61*(1), 27–57. <https://doi.org/10.1357/002224003321586408>
- Stommel, H. (1948). The westward intensification of wind-driven ocean currents. *Eos, Trans. Amer. Geophys. Union*, *29*(2), 202–206. <https://doi.org/10.1029/TR029i002p00202>
- Thompson, A. F., Speer, K. G., & Schulze Chretien, L. M. (2020). Genesis of the Antarctic Slope Current in West Antarctica. *Geophysical Research Letters*, *47*(16), e2020GL087802. <https://doi.org/10.1029/2020GL087802>
- Tozer, B., Sandwell, D. T., Smith, W. H. F., Olson, C., Beale, J. R., & Wessel, P. (2019). Global bathymetry and topography at 15 arc sec: SRTM15+. *Earth and Space Science*, *6*(10), 1847–1864. <https://doi.org/10.1029/2019EA000658>
- Vallis, G. K. (2017). *Atmospheric and oceanic fluid dynamics*. Cambridge University Press.
- Waterman, S., Hogg, N. G., & Jayne, S. R. (2011). Eddy–Mean flow interaction in the Kuroshio extension region. *Journal of Physical Oceanography*, *41*(6), 1182–1208. <https://doi.org/10.1175/2010JPO4564.1>
- Xu, X., Chassignet, E. P., Firing, Y. L., & Donohue, K. (2020). Antarctic Circumpolar Current transport through Drake Passage: What can we learn from comparing high-resolution model results to observations? *Journal of Geophysical Research*, *125*(7), e2020JC016365. <https://doi.org/10.1029/2020JC016365>

References From the Supporting Information

- Stommel, H., & Veronis, G. (1980). Barotropic response to cooling. *Journal of Geophysical Research*, *85*(C11), 6661–6666. <https://doi.org/10.1029/JC085iC11p06661>